

# Astrophysical Fluids of Novae: High Resolution Pre-decay X-ray spectrum of V4743 Sagittarii

J.M Ramírez-Velasquez

**Abstract** Eight X-ray observations of V4743 Sgr (2002), observed with *Chandra* and *XMM-Newton*, are presented, covering three phases: Early optically thin hard emission (day 50.2), photospheric emission from the ejecta (days 180.4, 196.1, 301.9, 371, 526), and faint post-outburst emission (days 742 and 1286). The flux level at Earth during the first and last phase is of order  $10^{-12}$  erg cm $^{-2}$  s $^{-1}$  over the energy range 0.3-2.5 keV. These values are higher than an upper limit obtained in September 1990 with ROSAT. The nova thus continued fading in the soft band (0.1-2.4 keV). The nova turned off some time between days 301.9 and 371, and the X-ray flux subsequently decreased from day 301.9 to 526, following an exponential decline time scale of  $(96 \pm 3)$  days. We use the absorption lines present in the SSS spectrum for diagnostic purposes, and characterize the physics and the dynamics of the expanding atmosphere during the explosion of the nova. The information extracted from this first stage is then used as input for computing full photoionization models of the ejecta in V4743 Sgr. The SSS spectrum is modeled with a simple black-body and multiplicative Gaussian lines, which provides us of a general kinematical picture of the system, before it decays to its faint phase (Ness et al. 2003). In the grating spectra taken between days 180.4 and 370, we can resolve the line profiles of absorption lines arising from H-like and He-like C, N, and O, including transitions involving higher principal quantum numbers. Except for a few interstellar lines, all lines are significantly blue-shifted, yielding velocities between 1000 and 6000 km s $^{-1}$  which implies an ongoing mass loss. It is shown that significant expansion and mass loss occur during this phase of the explosion, at a rate  $\dot{M} \approx (3 - 5) \times 10^{-4} (\frac{L}{L_{38}}) M_{\odot}/yr$ . Our measurements show that the efficiency of the amount of energy used for the motion of the ejecta, defined as the ratio between the kinetic luminosity  $L_{kin}$  and the radiated luminosity  $L_{rad}$ , is of the order of one.

---

J.M Ramírez-Velasquez  
Physics Centre, Venezuelan Institute for Scientific Research (IVIC), PO Box 20632, Caracas 1020A,  
Venezuela - e-mail: josem@ivic.gob.ve

Departamento de Matemáticas, CINVESTAV del I.P.N., 07360 México, D.F., México.

## 1 Introduction

Classical Novae (CNe) are the historically longest-known eruptive sources in the sky. They occur in binary systems consisting of a white dwarf (WD) and a normal star with typical orbital periods of a few hours. Mass lost by the star leads to accumulation of a hydrogen-rich layer on the WD surface that erupts in a thermonuclear explosion after nuclear ignition conditions are reached (Starrfield and Swift-Nova-CV group (2008)). The radiative energy output of the outburst is large enough to eject both accreted material and some dredged up WD material into space. This envelope resembles a stellar atmosphere of an F giant (Payne-Gaposchkin (1964)). Early in the evolution, the ejecta are bright in the optical, and no high-energy radiation is expected. As the expansion continues, the density drops, the photosphere moves inward in mass, exposing successively hotter plasma, and the effective temperature rises. This process leads to the commonly observed decline in optical, while the peak of the spectral energy distribution (SED) moves to higher energies. In this standard picture, at some point in the evolution the peak is expected to reach the X-ray regime, and several novae have been observed to emit a supersoft X-ray spectrum, similar to those of the class of supersoft X-ray binary sources (SSS) such as Cal 83 (Starrfield et al. (2004)). These are extremely luminous sources ( $\log L_{\text{bol}} \approx 37$ ) with effective temperatures  $\sim 30 - 40 \text{ eV}$  ( $T_{\text{eff}} \approx (3 - 5) \times 10^5 \text{ K}$ ). Such high luminosities and temperatures, if observed in systems with WDs, can only be powered by nuclear burning, and when a nova is emitting an SSS spectrum, nuclear burning near the surface of the WD must still be continuing. The time at which a nova ceases to emit an SSS spectrum can be considered as the time when nuclear burning has turned off.

The first detailed X-ray study of a nova during outburst was carried out for V1974 Cyg (Krautter et al. (1996)). While X-ray emission was not expected to be observable before the photosphere receded to sufficiently hot layers within the envelope, V1974 Cyg exhibited an early hard X-ray spectrum, apparently with the characteristics of a collisional, optically-thin plasma (Krautter et al. (1996); Balman et al. (1998a)). Such early X-ray emission has now been seen in other novae, e.g., V838 Her (Lloyd et al. (1992)), V382 Vel (Orio et al. (2001)), several CNe in a sample of novae observed with *SWIFT* (Ness et al. (2007)), and, recently, V2491 Cyg (Page et al. (2010)), and V458 Vul (Tsujimoto et al. (2009)).

X-ray observations during the SSS phase yield a physical description of the innermost regions. X-ray spectra yielding color-equivalent temperatures in excess of  $\sim (2 - 3) \times 10^5 \text{ K}$  imply that nuclear burning is the energy source (Ness et al. (2008)). The evolution of the SSS is governed by the evolution of the nuclear-burning envelope that remains on top of the WD. Models of post-outburst WD envelopes with steady H-burning show that envelopes with smaller masses have smaller photospheric radii and higher effective temperatures. As the H-rich envelope mass decreases due to mass loss and conversion of H to He, the effective temperature is predicted to increase at constant bolometric luminosity, reaching maximum temperature just before turn-off. This has recently been observed by Page et al. (2010) in V2491 Cyg. The evolution of the effective temperature is faster at low tempera-

tures, slowing down at high temperatures, with its pace depending on the WD mass and the particular envelope composition (Sala and Hernanz (2005)). For data with sufficient signal-to-noise ratio and spectral resolution, non-LTE atmosphere models allow quantitative conclusions. However, Ness et al. (2009) found significant blue shifts in all available high-resolution X-ray spectra of novae, indicating continuing expansion and probably mass loss, such that rigorous application of such methods must include the expansion (van Rossum and Ness (2010)).

An alternative route is the use of expanding photoionized envelope models, for the characterization of the main kinematics and physical parameters of the system. And that is the main goal of the work we introduce in this chapter. Here, we present an analysis of the X-ray spectra from the *Chandra* and *XMM-Newton* monitoring observations of V4743 Sgr (2002) that were carried out between days 50.2 and 1286 after discovery.

## 2 Observations

Altogether, five observations with *Chandra* and three with *XMM-Newton* were obtained between days 50 and 1286 after outburst, probing different phases of the evolution. In Table 1 we list the journal of observations with day after discovery.

**Table 1** Observation summary

day <sup>a</sup>	ObsID	Detector/mode	Start date	Exp. time (ks)	count rate	flux <sup>h</sup>	flux <sup>i</sup>
50.23	3774	ACIS-S <sup>b</sup> /FAINT	2002-11-09.24	5.30	0.3 <sup>g</sup>	1.8 ± 0.6	1.3 ± 0.2
180.39 <sup>d</sup>	3775	HRC <sup>b</sup> /LETGS	2003-03-19.40	14.7	44.0 <sup>e</sup>	2022 ± 450	1815 ± 400
180.56 <sup>d</sup>	3775	HRC <sup>b</sup> /LETGS	2003-03-19.55	5.6	0.62 <sup>e</sup>	32 ± 15	24.1 ± 8
196.14	0127720501	RGS <sup>c</sup>	2003-04-04.93	35.2	51.9 <sup>f</sup>	1709 ± 573	1709 ± 573
301.88	3776	HRC <sup>b</sup> /LETGS	2003-07-18.90	11.7	43.5 <sup>e</sup>	2006 ± 190	1810 ± 170
370.98	4435	HRC <sup>b</sup> /LETGS	2003-09-25.99	12.0	22.6 <sup>e</sup>	1044 ± 350	928 ± 300
526.05	5292	HRC <sup>b</sup> /LETGS	2004-02-28.06	10.3	5.05 <sup>e</sup>	230 ± 40	172 ± 30
741.98	0204690101	MOS1 <sup>c</sup> /THIN	2004-09-30.77	22.1	0.086 <sup>g</sup>	2.6 ± 1.0	0.6 ± 0.3
1285.9	0304720101	MOS1 <sup>c</sup> /THIN	2006-03-28.64	34.1	0.055 <sup>g</sup>	1.5 ± 0.5	0.4 ± 0.2

<sup>a</sup>after discovery (2002, September 19.8)

<sup>b</sup>*Chandra*

<sup>c</sup>*XMM-Newton* (combined RGS1 and RGS2)

<sup>d</sup>observation split in high-state and low-state

<sup>e</sup>counts per second from dispersed photon in range 5 – 55 Å

<sup>f</sup>counts per second from dispersed photon in range 5 – 38 Å (RGS1)

<sup>g</sup>counts per second (0.2 – 10 keV = 1.2 – 62 Å)

<sup>h</sup>absorbed band flux [ranges as in footnotes e – g] in units 10<sup>-12</sup> erg cm<sup>-2</sup>s<sup>-1</sup>; error ranges represent peak to peak variations

<sup>i</sup>absorbed band flux [range 5 – 38 Å = 0.3 – 2.5 keV] in units 10<sup>-12</sup> erg cm<sup>-2</sup>s<sup>-1</sup>; error ranges represent peak to peak variations

## 2.1 Observing instruments

The ACIS-S is an array of CCD chips, sensitive between 0.1 – 10 keV with an effective area ranging from 110 – 600 cm<sup>2</sup> from 0.5 – 1.5 keV and an energy resolution of roughly 100 eV. The HRC (High-Resolution-Camera) is a microchannel plate imaging detector that records the dispersed photons of the Low Energy Transmission Grating Spectrometer (LETGS). The LETGS covers a wavelength range of 1 – 170 Å with an effective area of 10 – 30 cm<sup>2</sup> in the 19 – 40 Å range and a wavelength resolution of 0.05 Å. Since the dispersion angle is proportional to wavelength, the grating spectra are extracted in wavelength units. The Reflection Grating Spectrometer (RGS) on board *XMM-Newton* is sensitive between 1 – 38 Å with an effective area between 20 – 60 cm<sup>2</sup> in the 19 – 40 Å range and a wavelength resolution of 0.05 Å. The European Photon Imaging Camera (EPIC) consists of two MOS (Metal Oxide Semi-conductor) CCD detectors and a pn detector. The MOS are sensitive between 0.2-10 keV with an effective area ranging between 100 – 600 cm<sup>2</sup> from 0.5 – 1.5 keV and an energy resolution of roughly 50 eV.

## 2.2 Extraction procedures

The main observation product follows the concept of events files, which are tables of events with columns containing positions, arrival times and energies for each individual event. We generated these files from the raw products using standard reduction routines provided by the respective *Chandra* CIAO <sup>1</sup> (v4.2) software and *XMM-Newton* SAS (9.0.0). We extracted average count rates and spectra from the events files by application of filter criteria on photon positions, arrival times, and energy (see below). In the right part of Table 1 we give the count rates and absorbed X-ray band fluxes for the energy ranges indicated in the corresponding footnotes. Absorbed X-ray band fluxes can be obtained from spectral models with fairly good accuracy. As long as the spectra are reasonably well reproduced, the resultant flux does not depend strongly on the model assumptions, and the determination of absorbed fluxes over the energy band covered by the detector is thus robust. Nevertheless, for the grating spectra we made use of the high spectral resolution and determined the fluxes directly from the spectra by integrating the photon fluxes from each spectral bin in a given wavelength range. First, we extracted the fluxes from the entire band pass of each instrument, except for the LETGS fluxes, where significant contamination of second-order photons occurs longwards of 55 Å. For direct comparison of the brightness evolution, we also extracted fluxes over a common band pass for all observations. Since the light curves are highly variable, we consider the range between minimum and maximum count rates as uncertainty ranges. The extracted fluxes are listed in the last two columns of Table 1.

---

<sup>1</sup> <http://cxc.harvard.edu/ciao>

The first X-ray observation was made with low (CCD) spectral resolution with the original purpose to determine whether the brightness level was suitable for high-resolution observations. We have placed a circular extraction region with a radius of 20 pixels around the expected source position and extracted the number of counts in the detect cell. The background was extracted from an adjacent (source-free) region. As can be seen from Table 1, the source was clearly detected. Next, we extracted a spectrum from the photon energies. The spectral analysis is described in §6.1, and the fluxes listed in the last two columns of Table 1 have been directly integrated from the best-fit model.

The time period between days 50.2 and 180.4 was unfortunately not covered with any observations because Sagittarius was behind the Sun. As soon as V4743 Sgr was visible again, a bright SSS spectrum was observed by *Chandra* with high-amplitude oscillations and a sudden, unexpected decay by two orders of magnitude (Ness et al. (2003)). We split this observation into two parts (starting on days 180.4 and 180.6) in order to investigate the bright and faint phases separately. Three more *Chandra* LETGS observations were taken on days 301.9, 371, and 526. The spectrum was obtained by following the standard *Science Threads*<sup>2</sup> for extraction of LETG/HRC-S Grating spectra.<sup>3</sup> We use the new spectral extraction region (i.e., a “bow-tie” shaped region), contained in CALDB 4.2. When the LETG (*Low Energy Transmission Grating*) is used with the HRC-S detector (*High Resolution Camera*), this comprises a central rectangle abutted to outer regions whose widths increase as the dispersion distance increases. The background region is taken from above and below the dispersed spectra. The region shape for both, source and background negative and positive orders is precisely given in the CALDB V 4.2. Having properly extracted both, source and background spectra from each arm, we merged them, obtaining added source and background spectra. This is intended to increase the signal-to-noise ratio (S/N) of the final spectrum, and the spectral analysis (throughout this work) is based on this co-added spectrum.

The decay phase, which comprises the time interval before the faint-phase (obs day 180.6), of approximately 5 ks of duration, is discussed in Ness et al. (in prep.), and will not be analysed here. The pre-decay phase is composed then for the first 15 ks of the observation at day 180.4, which we call epoch 1. Due to similarities with this we also study the spectra at days 301 and 370 called epochs 2 and 3, respectively. The LETGS has an energy coverage range 0.07 – 10 keV, however, we make use of the energy bandpass 0.2 – 10 keV, since significant contamination of second and higher orders photons are expected below 0.2 keV. The final spectra is shown using a bin size of 0.0250 Å for epochs 1, 2, and the default bin size of the LEG 0.0125 Å for epoch 3, making use of the high resolution of the spectrometer.

On day 196.1, two weeks after the observation of the steep decay, an *XMM-Newton* ToO observation was carried out, and the nova was again bright in X-rays exhibiting a SSS spectrum. The spectra and count rates were extracted from standard pipeline products. We have corrected the RGS spectra for pile up by reclaiming the

---

<sup>2</sup> [http://cxc.harvard.edu/ciao/threads/spectra\\_letghrcs/](http://cxc.harvard.edu/ciao/threads/spectra_letghrcs/)

<sup>3</sup> Along with the calibration data CALDB V 4.2

first-order photons that were recorded in the second- and third-order RGS spectra. For the calculation of fluxes, we use the “fluxed” spectrum that combines RGS1 and RGS2 spectra. The “fluxed” RGS spectrum is a product of a SAS procedure that fully exploits the redundancy of the two spectrometers onboard *XMM-Newton*.

Two more observations were taken, on days 742 and 1286, with *XMM-Newton*. The RGS spectra do not contain sufficient signal for useful results, and we concentrate on the MOS1 observations. The source is not recorded in the pn detector because the source position coincided with a gap between two CCD chips. The count rates and spectra were extracted from the events file using circular extraction regions with a radius of 200 pixels, again filtering on the coordinates.

### 2.3 Brightness evolution

The evolution of the X-ray broad-band fluxes is depicted in the top panel of Fig. 1. From day 50.2 to 180.6, the flux increased by three orders of magnitude. The faint phase on day 180.6 yields a factor  $\sim 75$  reduced brightness compared to before the decay, but the flux level is still a factor  $\sim 20$  higher than the flux obtained from the pre-SSS observation taken on day 50.2 (see also Table 1). The flux on day 196.1 is slightly lower than the pre-decay flux, while we find the same flux level for day 301.9 as before the decay. We caution that the comparison of fluxes between days 180 and 196.1 is uncertain owing to cross-calibration uncertainties between different instruments and uncertainties arising from the pile up correction of the RGS spectrum. Note that the *Chandra* LETG spectra are not piled up because of the architecture of the HRC detector. The fluxes for days 301.9, 371, and 526.1 follow an exponential decline,  $e^{-t/\alpha}$ , with  $\alpha = (96 \pm 3)$  days ( $1-\sigma$  uncertainty).

The last two *XMM-Newton* observations taken on days 741 and 1286 yield fairly similar flux levels as on day 50.2. In order to determine whether this may be the quiescent level, we checked the ROSAT archive and found no X-ray detection in a 12-ks observation (ObsID 932149) taken 1990 September 17.1. The upper limit of  $2 \times 10^{-4}$  cps over the 0.1-2.4 bandpass corresponds to a *Chandra* and *XMM-Newton* count rate of  $< 10^{-3}$  cps and is thus well below the count rate level observed on days 50.2, 741, and 1286 encountered for the same band.

### 2.4 Spectral Evolution

As a first description of the spectral characteristics of the object, we extracted count rates from different energy ranges, and calculated two hardness ratios along the conventional definition  $HR = (H - S)/(H + S)$  with  $H$  and  $S$  being the count rates in two hard and soft bands, respectively. The evolution of the two different hardness ratios are shown in the second panel of Fig. 1, where the energy ranges for  $H$  and  $S$  are indicated in the bottom right legend. The evolution of both hardness ratios

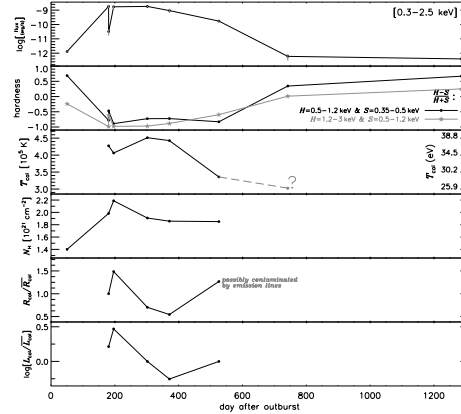


**Fig. 1** Evolution of X-ray band fluxes from the last column of Table 1 (top) and hardness ratios (second panel). The next four panels show the evolution of color-equivalent temperature, neutral hydrogen column density,  $N_{\text{H}}$ , effective radius, and bolometric luminosity. Only relative changes of radii and luminosities are shown because the absolute values are unreliable as a consequence of poor model assumptions. The value of the blackbody temperature found from the model to day 742. The Galactic absorption  $N_{\text{H}}$  obtained from the model to day 50.2 as described in §6.1 are included in the third and fourth panels, respectively. Since the blackbody temperature for day 742 is highly uncertain, it is marked with a gray question mark. The normalization for day 526 might be contaminated by emission lines, leading to an overestimated radius (5th panel).

demonstrates the three phases of evolution. We group the observations into an early hard spectrum (day 50), the Super Soft Source phase (days 180-370), and the post-SSS phase (days 526-1285). The panels below show the evolution of the spectral shape of the continuum color and related parameters characterizing the SSS spectra.

The detailed spectra are shown in Fig. 2 in the order of date after discovery from top to bottom (see upper right legends in each panel). While the grating spectra taken between days 180.4 and 526 can be converted to photon flux spectra, this is not possible for the CCD spectra, and the raw counts per bin are plotted instead. Since the CCD spectra are binned on an equidistant *energy* grid, these spectra are not equidistantly binned when plotted in wavelength units, which is chosen here for consistency with the majority of grating spectra. For orientation purposes, the corresponding energies to each given wavelength label on the x-axis are given in the top.

The spectral evolution of novae in X-rays can be divided into three major phases, which can be identified in Fig. 2: an early emission phase that is characterized by "hard" emission (day 50.2), the SSS phase (days 180.4 to 526), and a late emission phase that is again a harder spectrum (days 742 and 1286). While the SSS emission is photospheric emission from the extended WD, the origin of X-ray emission during the other two phases is less clear. Early "hard" emission is suspected to originate in shocks while the late emission phase could be radiatively cooling nebular ejecta.

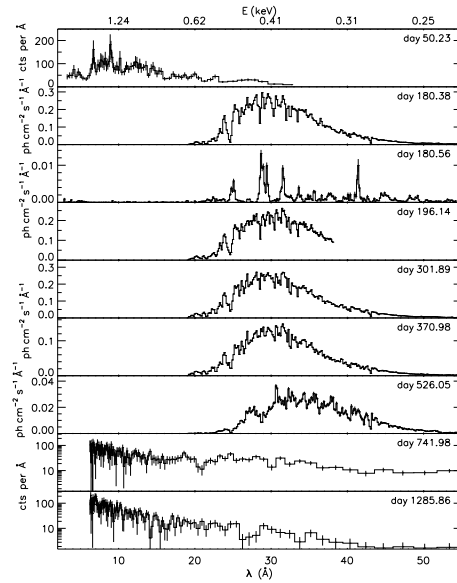


**Fig. 2** Comparison of all X-ray spectra with the start times given as fractional days after discovery in the upper right legend of each panel. For observation details see Table 1. The grating spectra were converted to photon fluxes (days 180.4-526), and data shortwards of  $19 \text{ \AA}$  were removed as no signal is present. The CCD spectra (days 50.2, 724, and 1286) have been extracted on an equidistant energy grid, but are shown on the same wavelength scale, and in units counts per  $\text{\AA}$ , without background subtraction. In the bottom two panels, the spectra are shown on a logarithmic scale.

The spectrum on day 50.2 is shown in the top panel of Fig. 2. It has very low signal to noise and spectral resolution but significant hard and soft emission can clearly be identified. Some of the features could be emission lines, and this spectrum thus meets expectations of an early hard emission line spectrum.

The LETGS spectrum taken on day 180.4 has already been presented by Ness et al. (2003). The spectrum is clearly significantly softer, and it is a continuum spectrum with absorption lines. On day 180.6, after the steep decay, an emission line spectrum has appeared (Ness et al. (2003)). As described above, units of photon fluxes are plotted.

The spectra taken on days 196, 302, 371, and 526 are remarkably similar, and they all originate from the extended WD photosphere. Small differences can be seen in the depth of some absorption lines, and the Wien tail extends to somewhat shorter wavelengths between days 196 and 372, compared to days 180.6 and 526. On day 526, the absorption lines are less deep, and emission line features arise. These emission lines could have been present all the time, and with the lower emission level of the continuum on day 526, they are easier to see. A detailed comparison of the SSS spectra can be found in §6.

The last two *XMM-Newton* observations are too faint for the high-resolution RGS, and only the low-resolution MOS1 spectra are useful. In the bottom two panels of Fig. 2, the spectra from days 742 and 1286 are shown. Both spectra show no features that could be associated with emission lines like in the ACIS spectrum in the top panel of Fig. 2. Since the MOS1 has a similar resolution as the ACIS, we can conclude that the post-outburst spectra are of a different nature.

#### 2.4.1 Continuum and detection of X-ray lines in the SSS spectrum

Here we describe the selection of the continuum and the statistical procedure for the detection of the X-ray lines. Motivated by Ness et al. 2010, we choose a black-body with temperature  $kT = 37$  eV ( $T = 427000$  K). The column density of neutral hydrogen in the line of sight,  $N_{\text{H}}$ , was found by comparison of the non-absorbed model with  $N_{\text{H}}$ -corrected observed spectra, from different assumed values of  $N_{\text{H}}$ . Other authors argued that  $\chi^2$  minimization of  $N_{\text{H}}$  overemphasizes the 25–35-Å region where the highest count rates are encountered, while the importance of  $N_{\text{H}}$  increases towards longer wavelengths, where the count rate is low, and the contributions to  $\chi^2$  are small. We use the `tbabs`<sup>4</sup> model for the interstellar absorption with a column density of  $N_{\text{H}} = 2.2 \times 10^{21} \text{ cm}^{-2}$ . For the continuum described above we look for significant residuals using as general strategy model comparison. The resulting value of  $2.2 \times 10^{21} \text{ cm}^{-2}$  is between expected values from Galactic neutral hydrogen maps. For the purposes of detecting a spectral feature, i.e., an absorption/emission line (in the count-wavelength space) is at least two *change points* (separated by at least a distance equivalent to the resolution of the instrument). In the statistics literature this is a point where the underlying process changes abruptly. The concept, has already been used in time series data (Scargle (2004)). Here we apply the idea to grating X-ray data. So we take a “chunk” of data, labeled  $k$ , and compute the marginalized likelihood of the model ( $M_k$ ) given the data ( $D_k$ ):

$$P(M_k|D_k) = P_0 \frac{\Gamma(N_k + \alpha)}{(\sum \Lambda_n + \beta)^{N_k + \alpha}}, \quad (1)$$

where  $N_k$  is the total counts in the chunk of data  $k$ .  $\Lambda_n$  is the broad band model count rate in units of counts per bin ( $n$ ).  $P_0$  forms part of the prior:

$$P_0 l^{\alpha-1} \exp(-\beta l), \quad (2)$$

where

$$P_0 = \frac{\beta^\alpha}{\Gamma(\alpha)}, \quad (3)$$

and  $\Gamma$  is the incomplete gamma function, and  $\beta$  and  $\alpha$  are parameters.

Our fitting of the continuum model into the data is made using the Interactive Spectral Interpretation System<sup>5</sup>, and the corresponding subroutines in the library

<sup>4</sup> The Tübingen-Boulder ISM absorption model

<sup>5</sup> <http://space.mit.edu/CXC/ISIS/>

package S-lang/ISIS Timing Analysis Routines<sup>6</sup>. Having computed the *change-points* of a feature, we take the wavelength center as an input for our CONTINUUM + LINES global model. The statistical significance is afterwards measured as the distance from the continuum to the core of the line, in units of the Poissonian error  $\sigma_p$ .

### 3 Fits to the SSS spectrum

Figure 3 shows the broad-band X-ray spectra of V4743 Sgr, by epoch, with the continuum described in §2.4.1 overplotted as a thick blue line. This continuum is then modified by multiplicative Gaussians:

$$M(E) = \exp\left(\tau \times \exp\left[-\frac{(E - E_0)^2}{(2\sigma^2)}\right]\right), \quad (4)$$

with

$$\tau = \frac{\tau_0}{\sqrt{(2\pi)\sigma}}. \quad (5)$$

Where  $\tau_0$  is the optical depth at the core of the line. The width is given by  $\sigma$ . And the energy at the core is  $E_0$ . The number of Gaussians to be used is given by the detection procedure described in §2.4.1, with  $\sigma_p \geq 2$ . The measurements of the line parameters along with their identifications are given in Table 4, corresponding to epoch 1 (other Tables are not shown for lack of space).

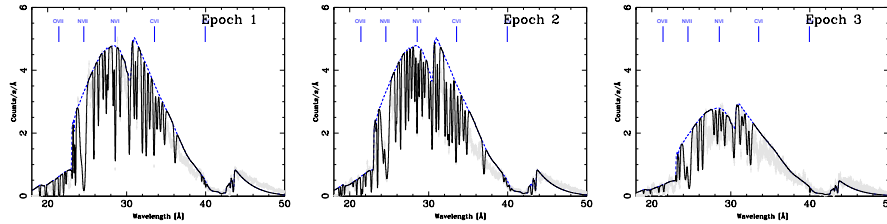


**Fig. 3** Chandra LETGS  $\pm 1$  order spectrum of V4743 Sgr, in the soft X-rays bandpass, for epochs (1,2,3). It is shown the black-body continuum as the thick solid line. The dashed line, is the global CONTINUUM + LINES model we use, in order to characterize the absorption of the system.

In the first column we have the observed center of the line, in the second column the statistical significance of the detection. In the third column, the candidate ionic specie for that line. In the fourth, the theoretical wavelength of the transition. In the fifth, the atomic transition of the line. In the sixth, the Doppler shift of the core of the line. In the seventh, the equivalent width of the line (EW) in milli-angstroms,

<sup>6</sup> <http://space.mit.edu/cxc/analysis/SITAR/>

computed with:

$$EW = \int \left[ 1 - \frac{F_g(E)}{F_c(E)} \right] dE, \quad (6)$$

where  $F_g(E) = F_c \times M(E)$ ,  $F_c(E)$  is the continuum at the energy  $E$ . The ion column densities ( $N_j$ ) are derived from the identifications in the Tables, assuming that the equivalent widths lie on the linear part of the curve of growth, and are quoted in column 8. That is we calculate  $N_j$ , from:

$$\frac{EW_\lambda}{\lambda} = \frac{\pi e^2}{m_e c^2} N_j \lambda f_{ij}, \quad (7)$$

where  $m_e$  is the electron mass,  $c$  the speed of light, and  $f_{ij}$ , the oscillator strength of the transition between levels,  $i$  and  $j$ .

#### 4 Kinematic modeling of the pre-decay phase

The SSS spectrum originates from the extended atmosphere of the white dwarf. This is a photoionized optically thick expanding wind (van Rossum and Ness (2010)). Here we start by constructing a kinematic model for such a wind, based on the observed spectra, and we use this model to extract various important physical parameters from the observations.

We assume spherically concentric shells photoionized by a simple blackbody with integrated 1 – 1000 Ryd luminosity  $L = 10^{37}$  erg s<sup>-1</sup>, and temperature of  $kT = 37$  eV, which form an expanding envelope. At this point, we do not solve the equations of radiative transfer between spherical clouds, but assume that there is a relation between radial location and velocity field, and the ionizing flux dilute only geometrically as  $\propto r^{-2}$ . The gas composition is made of H, He, C, N, O, Ne, Mg, Si, S, Ar, Ca and Fe. We use the abundances of Grevesse et al. (1996) in our models (and use the term *solar* for these abundances). From the continuity equation for a constant mass loss rate, we adopt a density profile for the expanding envelope as described by a beta-law,

$$w(x) = w_0 + (1 - w_0) \left( 1 - \frac{1}{x} \right)^\beta, \quad (8)$$

where  $w$  is the velocity of the wind normalized to the terminal velocity  $v_\infty$ ,  $w_0$  is the normalized velocity at the base of the wind and  $x$  is the distance normalized to the radius of the central core  $x = r/r_0$ . The parameter  $\beta$  is the quantity governing the slope of the velocity with the distance. The other function responsible for the variation of the optical depth with velocity is the ion density. This is given by

$$n_i(x) = A_E \times n_H(x) \times q_i, \quad (9)$$

where  $A_E = n_E/n_H$  is the abundance of the element with respect to H,  $q_i = n_i/n_E$  is the ionization fraction, and  $n_H(x)$  is the gas number density

$$n_H(x) = n_0 x^{-2} w^{-1} = \left( \frac{\dot{M}}{4\pi\mu m_H} r_0^{-2} v_\infty^{-1} \right) x^{-2} w^{-1} \quad (10)$$

where  $\dot{M}$  is the mass loss rate and  $\mu m_H$  is the average mass of the particles. At this point we need to adopt a model for the ionization balance. We assume that we can compute the ionization fraction  $q_i$  of each specie as a function of an ionization parameter  $\xi$  (the ratio of the ionizing flux  $F$  to the gas density  $n_H$ ) at each radial point.  $\xi$  for the optically thin case is

$$\xi = \frac{4\pi F}{n_H} = \frac{L_{ion}}{r^2 n_H}, \quad (11)$$

where  $L_{ion}$  is the ionizing luminosity of the source, but if the space between the source and the photoionized region is optically thick

$$\xi = \frac{4\pi F}{n_H} = \frac{L_{ion} \times \exp[-\tau(r)]}{r^2 n_H}, \quad (12)$$

where  $\tau(r)$  is the optical depth up to the observed gas. By combining equations (10) and (11)

$$\xi = \xi_0 \times \exp[-\tau(r)] w, \quad (13)$$

where  $\xi_0 = L_{ion}/(r_0^2 n_0)$ . This is what we call, a spherical wind, because the density profile is that of a spherically symmetric shell. Due to additional complexities that can be associated to the expansion of the nova and to take into account deformation of the density profile (due to magnetic fields for instance), we re-write the density as:

$$n_H(x) = n_0 x^{-2+\kappa} w^{-1}, \quad (14)$$

where a positive value of  $\kappa$  implies that the gas flow dilutes more slowly than in a free spherical expansion, i.e. that there are sources of gas embedded in the flow, or that the flow is confined. A negative value corresponds to sinks of gas in the flow, or expansion of an initially confined flow in a flaring geometry. Here and in what follows, we set  $w_0 = 0$  for simplicity. We then find that

$$\xi = \xi_0 \times \exp[-\tau(r)] w \times (1 - w^{1/\beta})^\kappa, \quad (15)$$

and this is the relationship between the ionization parameter and the radial velocity for a non-spherical, optically thick wind. The two panels in Figure 4 shows details of the spectrum and the results of our model. Most of the Gaussian features match well the observed spectrum, more specifically the centroids of the features are well located, a good element for our purposes. However, the fit is far from being statistically acceptable.

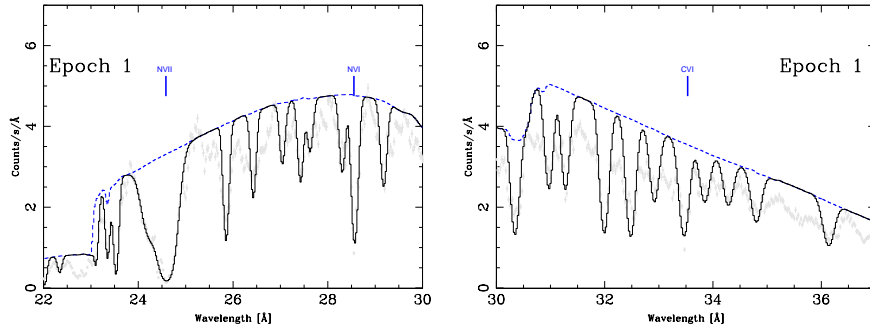


**Fig. 4** *Chandra* LETGS  $\pm 1$  order spectrum of Sgr. V4723, in the range 22-37 Å, for epoch 1. Several absorption features are identified and modeled with multiplicative Gaussians (solid line) modifying a blackbody continuum (dashed line).

### 5 Ionizing Luminosity, Mass Loss Rate, and Kinetic Luminosity of the Flow

We seek to constrain key physical parameters of the wind such as its mass loss rate and kinetic luminosity from the observed spectra and the relations derived above (see Table 2 for a summary). But, first one needs to answer a basic question, is the wind optically thin or optically thick?

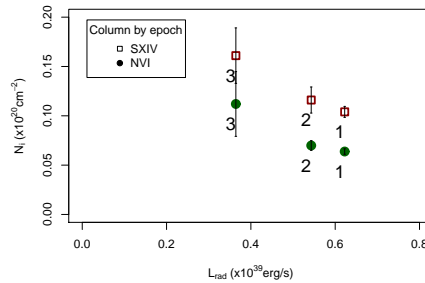


**Fig. 5** Column densities of S xvii and N vi resonant lines vs. apparent luminosity for the three epochs of observation. These two column densities are easily measured in the spectra and span a large range in ionization.

To answer this we look for possible changes in the ionization of the spectra among the three epochs of observation. In Figure 5 we look at the relative column densities of S xvii and N vi resonant lines vs. apparent luminosity for the three epochs of observation.

These two column densities are easily measured in the spectra and expand a large range in ionization. The ratio of column densities is notoriously flat, and so are the ionization of the spectra, while the apparent luminosity changes by a factor of  $\approx 2$ . This means that the three spectra steam from different radial distance, being the region farthest from the source in epoch 1 when the luminosity is maximum and nearest in epoch 3. It also means that if  $\xi$  is to remain constant for varying  $L_{rad}$  and the wind is spherical it cannot be optically thin, but thick (see equation 11).

**Table 2** Parameters of the system: Mass loss rate  $\dot{M}$ ,  $\dot{M}/L_{ion}$  and  $L_{kin}/L_{rad}$ .

Epoch	$\dot{M}^a$	$\dot{M}/L_{ion}^b$	$L_{kin}/L_{rad}$
I (C VI)	4.2	2.63	3.02587
I (N VI)	5.3	3.32	3.52105
I (O VII)	2.5	1.55	1.07782
II (C VI)	4.3	2.71	3.34455
II (N VI)	6.2	3.92	5.77883
II (O VII)	–	–	–
III (C VI)	–	–	–
III (N VI)	0.1	0.09	0.00007
III (O VII)	1.5	0.93	0.23078

(a) In units of  $\times 10^{-4} (\frac{L}{L_{38}}) M_{\odot}/yr$ . (b) In units of  $\times 10^{-16}$  gr/ergs.

From equations 10 and 12 one can write the mass loss rate as

$$\dot{M} = 4\pi\mu m_H L_{ion} \times \exp(-\tau) \left( \frac{v}{\xi} \right) \quad (16)$$

where  $\mu m_H$  is the average mass of the particles. The ratio  $(v/\xi)$  can be independently determined from observations for each of the species observed in the spectra. The values of  $v$  were measured from the centroids of the lines; C VI  $\lambda 33.734$ , N VI  $\lambda 28.787$  and O VII  $\lambda 21.602$  for the three epochs under consideration (see Tables 3 - 5). The values of  $\xi$  are taken from the ionization balance curves of Kallman and Bautista (2001). Figure 6 presents the results for  $\dot{M}$  as derived from different species and on different epochs. The spread in values from different species is probably due to variations in the optical depth up to the regions where different ions form. The optical depth  $\tau$  is a complex function that depends on the column density of gas and its physical conditions up to the region responsible for the observed absorption troughs. The overall results are for an upper limit to  $\dot{M} \approx 4 \times 10^{-4} (\frac{L}{L_{38}}) M_{\odot}/yr$ .

The kinetic energy of the flow is defined as

$$L_{kin} = \frac{1}{2} \dot{M} v^2. \quad (17)$$

Our results for the ratio of  $(L_{kin}/L_{rad}) \times \exp \tau$  in epochs 1 - 3 are depicted in Figure 7. The numeric values in this figure can be regarded as upper limits to the ratio of kinetic to radiative energy in the wind. Interestingly, this ratio is less than one

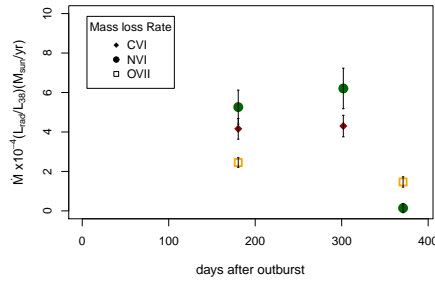


**Fig. 6** Mass loss rate during days 180.4, 301 and 371 after outburst. We use three spectral absorption lines to compute this quantity: C VI  $\lambda 33.734$ , N VI  $\lambda 28.787$  and O VII  $\lambda 21.602$ . Because of the luminosity is model-dependent,  $\dot{M}$  is give as a function of it.  $L_{38}$  is luminosity in units of  $10^{38}$  erg  $s^{-1}$ .

in epoch 3, suggesting that the flow has fallen out of equipartition. This can be understood if by this time in the expansion radiative pressure has become insufficient to overcome the gravitational potential. If this result is applicable to other novae it means that ejecta mass determinations based on the assumption of equipartition are only reliable when near the spectral peak, which is also the kinetic peak. During other phases, the mass outflow is very small.

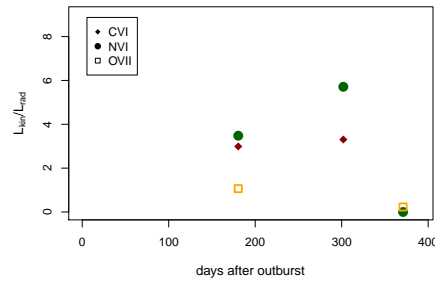


**Fig. 7** Efficiency of the amount of energy used for the motion of the ejecta, measured as the ratio between the kinetic luminosity  $L_{kin}$  and the radiated luminosity  $L_{rad}$ . We use three spectral absorption lines to compute this quantity: C VI  $\lambda 33.734$ , N VI  $\lambda 28.787$  and O VII  $\lambda 21.602$ . The three lines are consistent with an efficiency of the order of one. See text for details.

## 6 Analysis and discussion

Here we present an analysis and following of a discussion of the: (1) early hard spectrum, (2) sss-phase and (3) the post-sss phase.

### 6.1 Analysis of early hard spectrum

V4743 Sgr is not the first nova for which a hard X-ray spectrum was found before the WD has become visible in X-rays. Spectral model fits to such spectra imply that the X-ray emission originates from an optically thin collisional plasma, leading to the interpretation of shock fronts within the ejecta (O’Brien et al. (1994)).

For this reason, we chose a model that produces an emission line spectrum arising in an optically thin plasma with an isothermal electron temperature,  $T_e$ , in order to model the ACIS-S spectrum taken on day 50.2. We have used `xspec`<sup>7</sup> to fit the model to the data while accounting for all instrumental effects. The `vapec` model is based on atomic data calculated by the Astrophysical Plasma Emission Code (APEC, v1.3.; Smith et al. (2001)) and allows the abundances of He, C, N, O, Ne, Mg, Al, Si, S, Ar, Ca, Fe, and Ni to vary. The associated database, APED, is a more recent compilation of the atomic data contained in the MEKAL database which was used by Balman et al. (1998b) for the early emission of V1974 Cyg. The underlying assumptions are the same, i.e., the plasma is optically-thin and in collisional equilibrium. The principal parameters are temperature, normalization, and abundances relative to Solar. Since the plasma is unlikely to be isothermal, the sum of several APEC models can be used as an approximation of a continuous distribution of temperatures.

We have corrected for interstellar absorption assuming a fixed value of  $N_H = 1.4 \times 10^{21} \text{ cm}^{-2}$  (Lyke et al. (2002)), using the absorption model `tbabs`. The normalization parameter can be converted to volume emission measure ( $VEM$ , units  $\text{cm}^{-3}$ ), assuming a distance of 3.9 kpc. We found isothermal models statistically unsatisfactory with none achieving a reduced  $\chi^2$  better than  $\chi^2_{\text{red}} = 1.70$  (66 degrees of freedom,  $dof = N - n_p$ ). With 2-temperature (2- $T$ ) models, we found significantly better fits (see Table 3). For the best-fit model, we found an F-test value of 64 and a probability of  $1.8 \times 10^{-6}$ , thus the second model component is statistically justified. We found no further improvement with 3- $T$  models.

We first assumed solar abundances, scaled with a single factor for all abundances, but we found poor fits. Next we iterated the abundances of N, O, Ne, Mg, Si, S, and Fe, with other elements fixed at their solar values because no strong lines from these species are observable. The values of the abundances are poorly constrained. For Fe we find only an upper limit of  $< 0.04$ . We caution, however, that the low Fe abundance may be an artifact from approximating a continuous temperature distribution with only two isothermal components. Likewise, the abundances of the other

---

<sup>7</sup> <http://heasarc.nasa.gov/docs/xanadu/xspec/manual>

elements are poorly constrained, and no robust conclusions can be drawn from the best-fit values. The model parameters are listed in Table 3.

**Table 3** Models to ACIS spectrum (50.2 days after discovery)

Param.	Unit	Value <sup>a</sup>
$kT_1$	keV . . . . .	0.25 – 0.35
$\log(VEM_1)^c$	$\text{cm}^{-3}$ . . . . .	56.97 – 57.35
$kT_2$	keV . . . . .	2.7 – 15
$\log(VEM_2)^c$	$\text{cm}^{-3}$ . . . . .	56.05 – 56.28
$N_H$	$\text{cm}^{-2}$ . . . . .	$(1.4 \times 10^{21})^b$
flux <sup>d</sup>	$10^{-12} \text{ erg cm}^{-2} \text{ s}^{-1}$	1.2 – 2.4
$L_X^{c,d}$	$10^{32} \text{ erg s}^{-1}$ . . . . .	1.7 – 3.5
$\chi^2_{\text{red}} (dof)$	. . . . .	1.16 (64)

<sup>a</sup>90% uncertainty ranges

<sup>b</sup>fixed

<sup>c</sup>assuming distance 3.9 kpc

<sup>d</sup>0.2 – 10 keV

Abundances of N, O, Ne, Mg, Si, S, and Fe were varied (see text)

## 6.2 Discussion of early hard spectrum

The optically thin models used for fitting the early hard spectrum have originally been developed for the X-ray spectra of the Solar and stellar coronae. Our spectrum differs only in the X-ray luminosity and the likely different chemical composition of nova ejecta. The possibility could be considered that the early hard emission is of a similar origin. The Solar corona is powered by magnetic fields that are generated in the tachocline, the shear layers between the inner radiation zone and the outer convection zone. In a nova, magnetic fields could be generated by a similar dynamo, located in the interface between the ejected envelope and the WD surface that is rigidly rotating underneath the ejecta. If V4743 Sgr is an intermediate polar as suggested by Kang et al. (2006), and Dobrotka and Ness (2010), the permanent magnetic field of the WD could amplify dynamo-generated magnetic fields that power a corona. However, these considerations are solely based on plausibility arguments and are difficult to test, as no coherent models for the production of coronal emission exist. While the influence of magnetic fields can not necessarily be discarded, magnetic fields are not part of the models assumptions of the optically thin thermal models. Other possibilities can thus be considered.

More commonly accepted is the idea of interpreting the collisional nature as originating from a shock-heated plasma, although it is not clear whether the shocks originate from within the ejecta or from interactions with circumstellar material or the stellar wind of the companion.

Shocks with the stellar wind of the companion can only produce X-ray emission that is strong enough to be detectable at the given large distance if the stellar wind is sufficiently thick, and that requires a symbiotic nova such as RS Oph (Ness and Starrfield (2009)). In those systems, the companion is an evolved giant or subgiant. The ejecta run into this medium and dissipate some of their kinetic energy in the form of X-ray emission in the resulting shock (O’Brien et al. (1992)). In Classical Novae like V4743 Sgr, no strong stellar wind is present and no hard X-ray emission is expected from this production mechanism. One indication that V4743 Sgr is not a symbiotic nova is its short orbital period of 6.7 hours (Kang et al. (2006)), which is much shorter than typical orbital periods of symbiotic novae of several hundred days. We also consider shock interactions with circumstellar material unlikely, since the required density is higher than models of nova binary systems would suggest (Lloyd et al. (1992)). We have no reason to assume a higher density of the ambient medium as believed in GK Per (Bode (2004)) or V458 Vul (Tsujiimoto et al. (2009)), where a planetary nebula was found to surround the nova.

O’Brien et al. (1994) developed a shocked-gas model for the specific case of V838 Her and argued that the shock-heating must take place as a result of the interaction of different components *within* the ejecta. This “interacting winds” model has been refined by Lloyd et al. (1995). The complexity of the absorption lines that we found in the later SSS spectra indicates that the ejecta are not homogeneous, which is an important ingredient for this model. The presence of different velocity components could aid the development of shocks within the ejecta.

On the other hand, in order to produce enough X-ray emission in a shock, sufficiently high densities are needed, which unavoidably also have a high opacity. It has not been tested whether X-ray resonance lines of H-like ions can escape such a plasma. Furthermore, at least two distinct episodes of ejection are needed, providing slow-moving ejecta from an earlier outburst and fast-moving ejecta from a later ejection event. While this has been observed in V2362 Cyg, no explanation on how such secondary events could occur have been found. It could be possible, on the other hand, that some material is falling back, colliding with the expanding ejecta.

With all the given arguments, the cause for the early hard emission can not be identified with certainty. At this time, no deep X-ray spectrum of the early hard emission phase of a nova has been taken that could be used to pose constraints on the different causes.

### 6.3 Analysis of the SSS phase

The details of the grating spectra confront us with a high degree of complexity. The continuum has the shape of a stellar atmosphere in all observations between days 180.4 and 370, but the absorption lines are blue-shifted and highly structured. The blue-shifts of all photospheric lines indicate that expansion is still continuing during the SSS phase, bringing about (as we will show later) a significant mass loss (Ness et al. (2009)). The line profiles are extremely complex, and not all lines have

the same profile. Globally, up to three different velocity-bands can be observed:  $v_1 \sim -1000 \text{ km s}^{-1}$ ,  $v_2 \sim -2500 \text{ km s}^{-1}$  and  $v_3 \sim -6000 \text{ km s}^{-1}$ , coming from ionic species spanning a wide range of ionization states, from C v to S xiv (see Table 4).

**Table 4** Line properties of V4743 Sgr., LETGS epoch 1 (day 180.39).

$\lambda_{obs}^a$	$\sigma_p^b$	Ion <sup>c</sup>	$\lambda_0^d$	Atomic transition	Velocity (km s <sup>-1</sup> )	EW (mÅ)	$N_i^e$	flag
19.768 ± 0.003	8	N vii	19.826	1s <sup>2</sup> S - 4p <sup>2</sup> P	-873 ± 51	88 ± 10	0.52 ± 0.06	i
20.818 ± 0.003	10	N vii	20.910	1s <sup>2</sup> S - 3p <sup>2</sup> P	-1312 ± 45	98 ± 13	0.19 ± 0.03	i
21.470 ± 0.001	11	O vii	21.602	1s <sup>2</sup> 1S - 1s 2p <sup>1</sup> P	-1832 ± 16	104 ± 1	0.03 ± 0.01	s
22.021 ± 0.002	11	O vi	22.020	1s <sup>2</sup> 2s <sup>2</sup> S - 1s 2s(3P) 2p <sup>2</sup> P	11 ± 25	215 ± 31	0.05 ± 0.01	i
22.345 ± 0.004	12	O v	22.360	1s <sup>2</sup> 2s <sup>2</sup> 1S - 1s 2p <sup>1</sup> P	-334 ± 47	281 ± 76	NA	i
23.106 ± 0.001	20	N vi	23.277	1s <sup>2</sup> 1S - 1s 5p <sup>1</sup> P	-2202 ± 19	271 ± 30	2.00 ± 0.22	i
23.355 ± 0.002	17	O i	23.450	1s <sup>2</sup> 2s <sup>2</sup> 2p <sup>4</sup> - 1s 2s <sup>2</sup> 2p <sup>5</sup>	-1215 ± 20	291 ± 32	0.42 ± 0.05	g
23.534 ± 0.001	22	N vi	23.771	1s <sup>2</sup> 1S - 1s 4p <sup>1</sup> P	-2989 ± 13	257 ± 18	0.88 ± 0.06	i
24.604 ± 0.002	24	N vii	24.779	1s <sup>2</sup> S - 2p <sup>2</sup> P	-2121 ± 19	975	0.26 ± 1.86	s
25.856 ± 0.001	24	Ca xi	26.442	2p <sup>6</sup> 1S - 2p <sup>5</sup> 4s <sup>1</sup> P	-6644 ± 13	351 ± 20	1.50 ± 0.09	i
26.430 ± 0.002	20	Ca xi	26.962	2p <sup>6</sup> 1S - 2s 2p <sup>6</sup> 3p <sup>1</sup> P	-5915 ± 20	407 ± 35	0.17 ± 0.01	s
27.044 ± 0.003	21	Si xiii	27.341	1s 2s <sup>3</sup> S - 1s 4p <sup>3</sup> P	-3259 ± 31	452 ± 57	0.37 ± 0.05	i
27.429 ± 0.002	22	Ar xiv	27.464	2s <sup>2</sup> 2p <sup>2</sup> P - 2s <sup>2</sup> 3d <sup>2</sup> D	-382 ± 22	447 ± 41	0.04 ± 0.01	i
27.629 ± 0.003	18	Ar xiv	27.636	2s <sup>2</sup> 2p <sup>2</sup> P - 2s <sup>2</sup> 3d <sup>2</sup> D	-76 ± 36	480 ± 71	0.23 ± 0.03	i
28.309 ± 0.002	21	C vi	28.465	1s <sup>2</sup> S - 3p <sup>2</sup> P	-1645 ± 23	484 ± 46	0.51 ± 0.05	s
28.570 ± 0.001	29	N vi	28.787	1s <sup>2</sup> 1S - 1s 2p <sup>1</sup> P	-2261 ± 11	419 ± 18	0.06 ± 0.01	s
30.346 ± 0.002	21	S xiv	30.427	1s <sup>2</sup> 2s <sup>2</sup> S - 1s <sup>2</sup> 3p <sup>2</sup> P	-799 ± 15	507 ± 27	0.10 ± 0.01	s
30.975 ± 0.002	23	Si xii	31.012	1s <sup>2</sup> 2s <sup>2</sup> S - 1s <sup>2</sup> 4p <sup>2</sup> P	-359 ± 17	558 ± 33	0.44 ± 0.03	i
31.277 ± 0.002	26	N i	31.223	1s <sup>2</sup> 2s <sup>2</sup> 2p <sup>3</sup> - 1s 2s <sup>2</sup> 2p <sup>4</sup>	518 ± 18	572 ± 35	0.13 ± 0.01	g
31.996 ± 0.001	26	S xiii	32.239	2s <sup>2</sup> 1S - 2s 3p <sup>1</sup> P	-2261 ± 13	551 ± 23	0.10 ± 0.01	i
32.483 ± 0.001	24	Ca viii	32.770	3p <sup>2</sup> Po - ∞	-2626 ± 12	567 ± 24	0.21 ± 0.01	i
32.921 ± 0.002	19	Ca viii	33.120	3p <sup>2</sup> Po - ∞	-1801 ± 22	645 ± 45	NA	i
33.469 ± 0.002	26	C vi	33.734	1s <sup>2</sup> S - 2p <sup>2</sup> P	-2357 ± 16	619 ± 30	0.09 ± 0.01	i
33.850 ± 0.003	17	S xii	34.533	2s <sup>2</sup> 2p <sup>2</sup> P - 2s 2p(3P) 3p <sup>2</sup> D	-5928 ± 30	703 ± 67	0.12 ± 0.01	i
34.286 ± 0.004	16	C v	34.973	1s <sup>2</sup> 1S - 1s 3p <sup>1</sup> P	-5887 ± 34	727 ± 75	0.32 ± 0.03	i
34.799 ± 0.003	16	Ar ix	35.024	2p <sup>6</sup> 1S - 2p <sup>5</sup> 4d <sup>1</sup> P	-1926 ± 28	728 ± 60	0.10 ± 0.01	i
36.138 ± 0.003	15	S xii	36.398	2s <sup>2</sup> 2p <sup>2</sup> P - 2s <sup>2</sup> 3d <sup>2</sup> D	-2142 ± 27	764 ± 57	0.04 ± 0.01	i
39.508 ± 0.007	18	Mg x	39.668	1s <sup>2</sup> 2s <sup>2</sup> S - 1s <sup>2</sup> 5p <sup>2</sup> P	-1212 ± 54	266 ± 88	0.31 ± 0.10	i
40.012 ± 0.008	8	C v	40.268	1s <sup>2</sup> 1S - 1s 2p <sup>1</sup> P	-1905 ± 58	395 ± 80	0.03 ± 0.01	i
39.832 ± 0.006	9	Si xi	40.286	2s <sup>2</sup> 1S - 2p 3p <sup>3</sup> D	-3379 ± 46	68 ± 334	NA	i

Errors are  $1\sigma$ , computed individually for each of the parameters. (a) Observed wavelength in Å. (b) Statistical significance of the detection. (c) Probable ion identification. (d) The latest laboratory wavelength (in Å) taken from the National Institute of Standards and Technology (NIST: [http://physics.nist.gov/PhysRefData/ASD/lines\\_form.html](http://physics.nist.gov/PhysRefData/ASD/lines_form.html)). The K-shell wavelength of the oxygen ions (O vi and O v), are taken from García et al. (2005). (e) Measured column density for the ion in units of  $\times 10^{20} \text{ cm}^{-2}$ . (f) This is a broad feature, not actually associated to any atomic transition. Column flag: (s) Secure identification (i) Insecure identification (vi) Very insecure identification: means that there is no reliable atomic data for this ion. (g) Galactic line.

The distinctness of three velocity components as seen in Fig. 4, suggests that three (or more) concentric shells with low-density plasma in between are present. On the other hand, some lines are much narrower with only one or two components.

Clearly, not all lines originate from the same region, indicating that a large range of different plasma regions are visible at the same time.

The amount and duration of mass-loss during the SSS phase can only be determined from detailed, physically plausible models. NLTE effects have proven to be crucial Hartmann and Heise (1997), and minimum requisite of the model has to be that it is spherically symmetric and expanding van Rossum and Ness (2010). See also §4 for evidences of this latest assumption.

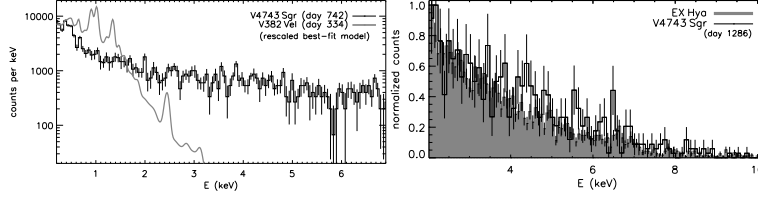


**Fig. 8** Comparison between the X-ray spectrum of V4743 Sgr taken on day 742 and a post-SSS nova spectrum (top) and that of the intermediate polar EX Hya (bottom). The thick grey line in the top panel is a rescaled best-fit model to an X-ray spectrum of V382 Vel taken 334 days after discovery after convolution through the MOS1 response. In the bottom panel, normalized counts from our MOS1 spectrum and a *SWIFT*/XRT count spectrum are compared.

#### 6.4 Discussion of the SSS phase

This is the first time that such results is extracted from observations, and a direct comparison with other works is not possible at the moment, but it implies that the kinematics of the ejecta comes from the radiation supplied by the central source; *suggesting the validity of the equipartition of energy* Shara et al. (2010a).

We assume an *ad hoc* efficiency of the radiation to ionization  $L_{\text{ion}}/L_{\text{rad}} = 0.41$ . A precise determination of  $L_{\text{rad}}$  is not simple, but we explore plausible values of it. We make use of the grid of novae models from Yaron et al. (2005), to estimate the mass of the white dwarf,  $M_{\text{WD}}$ , the temperature of its isothermal core,  $T_{\text{WD}}$ , and the mass transfer rate,  $\dot{M}_{\text{WD}}$ . If we take the average of  $m_{ej} \approx 4 \times 10^{-4} M_{\odot}$  (assuming  $L = 10^{38} \text{ erg s}^{-1}$ ), and look for the “best”-fit with the  $m_{ej}$  in Table 2 of Yaron et al. (2005), we find that the best- set of parameters is:  $M_{\text{WD}} = 0.4$ ,  $T_{\text{WD}} = 10^7 \text{ K}$  and  $\log_{10}(\dot{M}_{\text{WD}}) = -9 (M_{\odot}/\text{yr})$ . That would imply that we are in the presence of a low-mass ( $\lesssim 0.5 M_{\odot}$ ) WD close binary system Yaron et al. (2005). On the other hand, if we look for parameters with  $m_{ej} \approx 6 \times 10^{-4} M_{\odot}$ , then  $M_{\text{WD}} = 0.65$ ,  $T_{\text{WD}} = 10^7 \text{ K}$  and  $\log_{10}(\dot{M}_{\text{WD}}) = -12 (M_{\odot}/\text{yr})$ . However assuming we take our computed luminosity of  $L \approx 6 \times 10^{38} \text{ erg s}^{-1}$ , then our estimation of  $m_{ej}$ , would be  $\approx 2 \times 10^{-3} M_{\odot}$  and the extended grid of models Shara et al. (2010b) is required instead. In that case  $M_{\text{WD}} = 0.5$ ,  $T_{\text{WD}} = 3 \times 10^6 \text{ K}$  and  $\dot{M}_{\text{WD}} = 5 \times 10^{-11} (M_{\odot}/\text{yr})$ , posing our object at the border of a very luminous red novae. This is certainly an upper limit since

$L \approx 6 \times 10^{38} \text{ erg s}^{-1}$  is only for epoch 1 and not for the whole time-interval of the mass loss. At the moment more precise estimations of the luminosity are required to characterize the set of physical parameters of the system V4743 Sgr. More work on that regard might take place in the near future.

### 6.5 Discussion Post SSS phase

The basic idea of the final stages of nova evolution is that the ionized ejecta are radiatively cooling. Kinetic energy is successively converted to radiation via bound-bound collisional excitations followed by radiative deexcitations. As discussed in §6.2, charge exchange may also be an efficient cooling mechanism. In any way, the typical spectrum of a radiatively cooling plasma is an emission line spectrum, and appropriate models are thin-thermal models as, e.g., implemented in the *apex* module in *xspec*.

A good example of a spectrum of radiatively cooling ejecta are post-SSS *Chandra* observations of the nova V382 Vel, taken on days 268, 334, and 450 after discovery. The first of these spectra was analyzed by Ness et al. (2005), and the assumption of a radiatively cooling plasma proved valid. The other two observations were successfully modeled with thin-thermal plasma models by Burwitz et al. (2002), who also found a slow power-law decline from all three observations.

Both post-SSS spectra of V4743 Sgr are different to V382 Vel. In order to compare these spectra, we show in the top panel of Fig. 8 the *XMM-Newton*/MOS1 spectrum of V4743 Sgr taken on day 742 and a rescaled model that fits the *Chandra* spectrum of V382 Vel, taken on day 334, after convolution through the instrumental response of the MOS1 detector. The spectrum of V382 Vel contains strong emission lines that are resolvable with the MOS1 detector, and no significant emission arises above  $\sim 2 \text{ keV}$ . Meanwhile, our spectrum is dominated by featureless emission, including a hard tail extending up to  $10 \text{ keV}$ . We were unable to find a satisfactory fit to the spectrum using an optically thin, thermal plasma model. Furthermore, no significant fading of the hard emission can be identified between days 742 and 1286 (see Fig.9), while considerable fading was seen in V382 Vel (Burwitz et al. (2002)). All evidence we have thus indicates that the hard component is not typical post-nova emission.

It is also of interest to note that no X-ray emission was seen in a deep ROSAT observation in 1990, twelve years before outburst. The nova has thus not returned to quiescence yet. Since the ROSAT band only covers the energy range  $0.1\text{-}2.4 \text{ keV}$ , this non-detection only indicates the absence of soft emission, while the hard tail could have been present at that time. We thus predict that at least the soft component will eventually disappear.

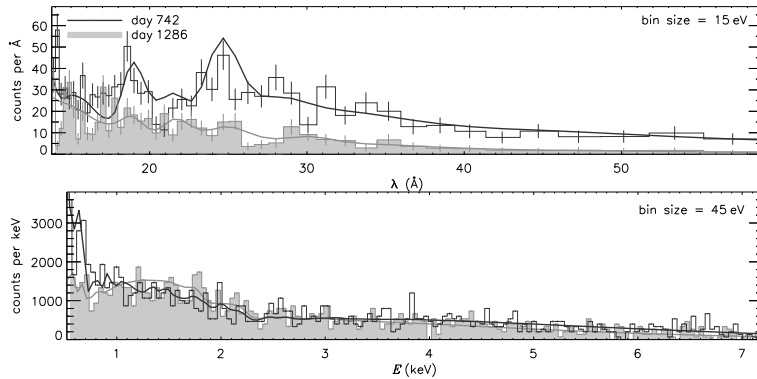


**Fig. 9** *XMM-Newton*/MOS1 spectra taken on days 742 and 1286, plotted with dark and light colors, respectively (see top left legend). In the top panel, the soft part is shown in units wavelength, and in the bottom part the hard part in units keV. Best-fit models are included with continuous lines.

## 7 Summary and Conclusions

We studied the hardness and brightness evolution using eight X-ray observations of V4743 Sgr and found three main stages of evolution.

(1) One X-ray spectrum was taken during the first phase and is an optically thin emission line spectrum which can be modeled by a thin-thermal plasma model, indicating that collisional processes are involved. Shock interactions of different components within the ejecta are the most commonly accepted model, but the presence of strong magnetic fields could lead to coronal emission that is heated in magnetically confined loops, similar to stellar coronae. V4743 Sgr has been proposed to be an intermediate polar, and we found supporting evidence (see below), thus magnetic fields may be present and relevant.

(2) The five high-resolution spectra obtained during the brightest SSS phase provide the largest amount of detail. The spectrum resembles a stellar atmosphere, but the absorption lines are blue shifted, and their complex profiles indicate that we are dealing with an expanding atmosphere, and the ejecta are inhomogeneous. Our technique of line identification, allow us to identify lines coming from H- and He-like ions of C,N,O blueshifted by  $\sim 2500 \text{ km s}^{-1}$ , lead us to estimate a mass loss rate of  $\dot{M} \approx (3 - 5) \times 10^{-4} \left(\frac{L}{L_{38}}\right) M_{\odot}/\text{yr}$ . The total ejected mass is  $m_{\text{ej}} \approx (2 - 3) \times 10^{-4} M_{\odot}$ , which locate V4743 Sgr., as a low-mass WD CO system. However due to uncertainties in the intrinsic luminosity of the source others (extreme?) positions in the parameter space of the grid of classical novae models, cannot be ruled out.

(3) The final phase is different from that observed in other novae, for which radiative cooling of the ionized ejecta has been observed. While significant fading of emission below  $\sim 2 \text{ keV}$  is seen, the harder part of the spectrum does not change and resembles that of the intermediate polar EX Hya. ROSAT has detected no soft X-ray emission before the outburst that could have swept away material that blocks all soft

emission. As this material replenishes, all emission below 2 keV might eventually disappear. This can be tested with further observations. Meanwhile, the hard emission could stay, which would support the intermediate polar nature of V4743 Sgr.

**acknowledgments** The author is indebted to J.-U. Ness and M. Bautista for important discussions, carried out in Berlin (AIP, Germany) and Kalamazoo (WMU, EEUU), very useful for the realization of this work. This contribution is partially supported by ivic (Venezuela) project 2013000259. Also, it was partially supported by ABACUS, CONACyT (Mexico) grant EDOMEX-2011-C01-165873.

## References

- S. Starrfield and Swift-Nova-CV group. Classical Novae in the Swift Era. In *AAS/High Energy Astrophysics Division*, volume 10 of *AAS/High Energy Astrophysics Division*, pages 19.04–+, March 2008.
- C. Payne-Gaposchkin. *The galactic novae*. 1964.
- S. Starrfield, F. X. Timmes, W. R. Hix, E. M. Sion, W. M. Sparks, and S. J. Dwyer. Surface Hydrogen-burning Modeling of Supersoft X-Ray Binaries: Are They Type Ia Supernova Progenitors? *Astrophysical Journal Letters*, 612:L53–L56, September 2004. doi: 10.1086/424513.
- J. Krautter, H. Oegelman, S. Starrfield, R. Wichmann, and E. Pfeffermann. ROSAT X-Ray Observations of Nova V1974 Cygni: The Rise and Fall of the Brightest Supersoft X-Ray Source. *Astrophysical Journal*, 456:788–+, January 1996. doi: 10.1086/176697.
- S. Balman, J. Krautter, and H. Oegelman. The X-Ray Spectral Evolution of Classical Nova V1974 Cygni 1992: A Reanalysis of the ROSAT Data. *Astrophysical Journal*, 499:395–+, May 1998a. doi: 10.1086/305600.
- H. M. Lloyd, T. J. O’Brien, M. F. Bode, P. Predehl, J. H. M. M. Schmitt, J. Truemper, M. G. Watson, and K. A. Pounds. X-ray detection of Nova Herculis 1991 five days after optical outburst. *Nature*, 356:222–224, March 1992. doi: 10.1038/356222a0.
- M. Orío, A. Parmar, R. Benjamin, L. Amati, F. Frontera, J. Greiner, H. Ögelman, T. Mineo, S. Starrfield, and E. Trussoni. The X-ray emission from Nova V382 Velorum - I. The hard component observed with BeppoSAX. *MNRAS*, 326:L13–L18, September 2001. doi: 10.1046/j.1365-8711.2001.04448.x.
- J.-U. Ness, G. J. Schwarz, A. Retter, S. Starrfield, J. H. M. M. Schmitt, N. Gehrels, D. Burrows, and J. P. Osborne. Swift X-Ray Observations of Classical Novae. *Astrophysical Journal*, 663:505–515, July 2007. doi: 10.1086/518084.
- K. L. Page, J. P. Osborne, P. A. Evans, G. A. Wynn, A. P. Beardmore, R. L. C. Starling, M. F. Bode, A. Ibarra, E. Kuulkers, J.-U. Ness, and G. J. Schwarz. Swift observations of the X-ray and UV evolution of V2491 Cyg (Nova Cyg 2008 No. 2). *MNRAS*, 401:121–130, January 2010. doi: 10.1111/j.1365-2966.2009.15681.x.

- M. Tsujimoto, D. Takei, J. J. Drake, J.-U. Ness, and S. Kitamoto. X-Ray Spectroscopy of the Classical Nova V458 Vulpeculae with Suzaku. *PASJ*, 61:69–+, January 2009.
- J.-U. Ness, G. Schwarz, S. Starrfield, J. P. Osborne, K. L. Page, A. P. Beardmore, R. M. Wagner, and C. E. Woodward. V723 CASSIOPEIA Still on in X-Rays a Bright Super Soft Source 12 Years after Outburst. *Astronomical Journal*, 135: 1328–1333, April 2008. doi: 10.1088/0004-6256/135/4/1328.
- G. Sala and M. Hernanz. Envelope models for the supersoft X-ray emission of V1974 Cyg. *A&A*, 439:1057–1060, September 2005. doi: 10.1051/0004-6361:20042587.
- J.-U. Ness, J. J. Drake, A. P. Beardmore, D. Boyd, M. F. Bode, S. Brady, P. A. Evans, B. T. Gaensicke, S. Kitamoto, C. Knigge, I. Miller, J. P. Osborne, K. L. Page, P. Rodriguez-Gil, G. Schwarz, B. Staels, D. Steeghs, D. Takei, M. Tsujimoto, R. Wesson, and A. Zijlstra. Swift X-Ray and Ultraviolet Monitoring of the Classical Nova V458 Vul (Nova Vul 2007). *Astronomical Journal*, 137:4160–4168, May 2009. doi: 10.1088/0004-6256/137/5/4160.
- D. R. van Rossum and J.-U. Ness. Expanding atmosphere models for SSS spectra of novae. *Astronomische Nachrichten*, 331:175–+, 2010. doi: 10.1002/asna.200911321.
- J.-U. Ness, S. Starrfield, V. Burwitz, R. Wichmann, P. Hauschildt, J. J. Drake, R. M. Wagner, H. E. Bond, J. Krautter, M. Orio, M. Hernanz, R. D. Gehrz, C. E. Woodward, Y. Butt, K. Mukai, S. Balman, and J. W. Truran. A Chandra Low Energy Transmission Grating Spectrometer Observation of V4743 Sagittarii: A Supersoft X-Ray Source and a Violently Variable Light Curve. *Astrophysical Journal Letters*, 594:L127–L130, September 2003. doi: 10.1086/378664.
- J. D. Scargle. Data Analysis Through Segmentation: Bayesian Blocks and Beyond. In *Bulletin of the American Astronomical Society*, volume 36 of *Bulletin of the American Astronomical Society*, pages 1200–+, August 2004.
- N. Grevesse, A. Noels, and A. J. Sauval. Standard Abundances. In *Astronomical Society of the Pacific Conference Series*, page 117, 1996.
- T. Kallman and M. Bautista. Photoionization and High-Density Gas. *Astrophysical Journal, Supplement*, 133:221–253, March 2001.
- T. J. O’Brien, H. M. Lloyd, and M. F. Bode. An interacting winds model for the X-ray emission from V838 Her (Nova Herculis 1991). *MNRAS*, 271:155–160, November 1994.
- R. K. Smith, N. S. Brickhouse, D. A. Liedahl, and J. C. Raymond. Collisional Plasma Models with APEC/APED: Emission-Line Diagnostics of Hydrogen-like and Helium-like Ions. *Astrophysical Journal Letters*, 556:L91–L95, August 2001. doi: 10.1086/322992.
- S. Balman, J. Krautter, and H. Oegelman. The X-Ray Spectral Evolution of Classical Nova V1974 Cygni 1992: A Reanalysis of the ROSAT Data. *Astrophysical Journal*, 499:395–+, May 1998b. doi: 10.1086/305600.
- J. E. Lyke, M. S. Kelley, R. D. Gehrz, and C. E. Woodward. Free-Free Turnover in Nova V4743 Sgr 2002 #3. In *Bulletin of the American Astronomical Soci-*

- ety, volume 34 of *Bulletin of the American Astronomical Society*, pages 1161–+, December 2002.
- T. W. Kang, A. Retter, A. Liu, and M. Richards. Nova V4743 Sagittarii 2002: An Intermediate Polar Candidate. *Astronomical Journal*, 132:608–613, August 2006. doi: 10.1086/505174.
- A. Dobrotka and J.-U. Ness. Multifrequency nature of the 0.75 mHz feature in the X-ray light curves of the nova V4743 Sgr. *MNRAS*, 405:2668–2682, July 2010. doi: 10.1111/j.1365-2966.2010.16654.x.
- J.-U. Ness and S. Starrfield. The X-ray Spectra of the Shock Systems in RS Oph. In S. J. Murphy & M. S. Bessell, editor, *Astronomical Society of the Pacific Conference Series*, volume 404 of *Astronomical Society of the Pacific Conference Series*, pages 77–+, August 2009.
- T. J. O’Brien, M. F. Bode, and F. D. Kahn. Models for the remnants of recurrent novae. III - Comparison with the X-ray observations of RS Ophiuchi (1985). *MNRAS*, 255:683–693, April 1992.
- M. F. Bode. The Evolution of Nova Ejecta. In M. Meixner, J. H. Kastner, B. Balick, & N. Soker, editor, *Asymmetrical Planetary Nebulae III: Winds, Structure and the Thunderbird*, volume 313 of *Astronomical Society of the Pacific Conference Series*, pages 504–+, July 2004.
- H. M. Lloyd, T. J. O’Brien, and M. F. Bode. Interacting Winds in Classical Nova Outbursts. *Ap&SS*, 233:317–321, November 1995. doi: 10.1007/BF00627366.
- J. García, C. Mendoza, M. A. Bautista, T. W. Gorczyca, T. R. Kallman, and P. Palmeri. K-Shell Photoabsorption of Oxygen Ions. *Astrophysical Journal, Supplement*, 158:68–79, May 2005. doi: 10.1086/428712.
- H. W. Hartmann and J. Heise. Hot high-gravity NLTE model atmospheres as soft X-ray sources. *A&A*, 322:591–597, June 1997.
- M. M. Shara, O. Yaron, D. Prialnik, and A. Kovetz. Non-equipartition of Energy, Masses of Nova Ejecta, and Type Ia Supernovae. *Astrophysical Journal Letters*, 712:L143–L147, April 2010a. doi: 10.1088/2041-8205/712/2/L143.
- O. Yaron, D. Prialnik, M. M. Shara, and A. Kovetz. An Extended Grid of Nova Models. II. The Parameter Space of Nova Outbursts. *Astrophysical Journal*, 623:398–410, April 2005. doi: 10.1086/428435.
- M. M. Shara, O. Yaron, D. Prialnik, A. Kovetz, and D. Zurek. An Extended Grid of Nova Models. III. Very Luminous, Red Novae. *ArXiv e-prints*, September 2010b.
- J.-U. Ness, S. Starrfield, C. Jordan, J. Krautter, and J. H. M. M. Schmitt. An X-ray emission-line spectrum of Nova V382Velorum 1999. *MNRAS*, 364:1015–1024, December 2005. doi: 10.1111/j.1365-2966.2005.09664.x.
- V. Burwitz, S. Starrfield, J. Krautter, and J.-U. Ness. Chandra ACIS-I and LETGS X-ray observations of Nova 1999 Velorum (V382 Vel). In M. Hernanz & J. José, editor, *Classical Nova Explosions*, volume 637 of *American Institute of Physics Conference Series*, pages 377–380, November 2002. doi: 10.1063/1.1518233.